Burn phase calculations and one-dimensional optimization studies for an inverse *z*-pinch magnetized target fusion system

2011 Plasma Phys. Control. Fusion 53 085013

(http://iopscience.iop.org/0741-3335/53/8/085013)

Plasma Phys. Control. Fusion **53** (2011) 085013 (23pp) doi:10.1088/0741-3335/53/8/085013

Burn phase calculations and one-dimensional optimization studies for an inverse z-pinch magnetized target fusion system

P V Subhash[1], S Madhavan[2], N Sakthivel[2], V Mishra[2], Aaditya V Majalee[2], P Pahari[2] and S Chaturvedi[2]

[1] Institute for Plasma Research, Gandhinagar-382 428, Gujarat, India
[2] Computational Analysis Division, B.A.R.C., Visakhapatnam-530012, India

E-mail: getsubhash@gmail.com and shashankvizag@gmail.com

Received 21 June 2010, in final form 28 February 2011
Published 16 June 2011
Online at stacks.iop.org/PPCF/53/085013

Abstract

This paper reports a computational optimization study for an inverse z-pinch magnetized target fusion system (MTF). This has been carried out by varying various parameters such as the magnetizing current, the initial liner radius and thickness, liner length, etc. One-dimensional (1D) magneto-hydrodynamic (MHD) calculations are used for this purpose. Capacitor bank parameters are held constant, as is also the inner conductor radius. The Kadomtsev stability parameter Q_0 is kept constant at 0.9 and the maximum plasma β at 0.4. The optimization study has yielded several parametric sets with an energy gain of more than unity, i.e. fusion energy output that exceeds the initial energy in the capacitor bank. A physical explanation for the local optimal points is provided through an energy flow analysis. For one case with energy gain exceeding unity, a simple liner stability analysis has been performed. This involves analytical calculations of the time points at which different liner modes become unstable. For these analytical studies, time-dependent parameters, such as liner acceleration, effective thickness of the liner region that still remains solid, and effective material strength, are obtained from 1D MHD simulations.

1. Introduction

Magnetized target fusion (MTF) is an alternative scheme for controlled thermonuclear fusion [1, 2]. It involves compression of a preheated, magnetized 'target' plasma by the electromagnetic implosion of a thin metallic liner. Liner implosion typically takes place in a z-pinch configuration during the so-called 'compression phase'. Near-adiabatic compression of the plasma also produces significant heating. Under suitable conditions, the plasma can be compressed and heated to fusion conditions, with a significant part of the liner kinetic energy

being converted to thermal energy of the plasma. The resulting fusion power output during the 'burn phase' rapidly heats the plasma to much higher temperatures, and the resulting pressure produces rapid expansion. The 'dwell time' of the liner near peak compression, and the final fuel density and temperature, must be designed to yield significant fusion energy generation [3]. The presence of a magnetic field in the target plasma reduces thermal conduction losses from the target plasma [2], but the resulting magnetic pressure also produces a retarding force on the imploding liner.

A detailed description of the concept, followed by a parametric study, can be obtained from [2]. A variety of MTF configurations being studied around the world, and their relative merits, are summarized in [3]. Computational studies of various MTF configurations have been reported in [1, 3–5]. A brief summary of such work is given in [6], and is omitted here for the sake of brevity. Compression of plasma to the megabar (million atmosphere) pressure range using metallic liners has been reported by Degnan *et al* [7]. The utility of various liner types has been studied by Ryutov [8]. Chittenden [9] reported results of plasma formation and implosion structure in wire array z-pinches and proposed a scheme called a 'double-ended' vacuum hohlram [10]. A theoretical study of plasma–wall interaction in such systems is reported in [11]. A summary of the computational studies for MTF has been reported by Sheehey *et al* [3]. The possibility of wall confinement of the plasma is discussed by Vekshtein [12]. A convective plasma cooling study is reported in [13], and the importance of radiation in plasma–wall interactions has been studied by Garanin *et al* [14]. Numerical simulations for cylindrical liner implosion on laser preheated targets are reported in [16]. This study indicates such a concept may yield a reasonable energy gain.

The concept of inverse z-pinch was initially presented and studied by Anderson *et al* in 1958 [17]. Special stability properties of the inverse z-pinch over conventional z-pinches are reported in [18]. The shock heating mechanism of inverse z-pinch and its dependence on pre-ionization levels are studied in [19].

Experimental and computational studies for plasma formation in the metal liner, due to diffusion of magnetic flux, have been reported in [15]. Thermal transport constitutes an important energy loss mechanism from the plasma to the liner and leads to the formation of a low-temperature cold plasma layer near the inner surface of the liner. A computational study of cold layer evolution during different phases of implosion has been reported in [20]. An analytical study of stationary cylindrical high pressure hot plasma columns surrounded by low temperature gas has been reported in [21]. That study focused on thermal losses from the plasma to outside surfaces through the low-temperature insulation layer across a magnetic field.

For a given pulsed-power driver, e.g. a capacitor bank with specified parameters, it is necessary to optimize the MTF system so as to maximize the total fusion energy output. This is a multi-variable optimization, involving the dimensions of the MTF system, the initial magnetic field and other parameters of the target plasma, spatial profiles of pressure and magnetic field through the target plasma, and so on. Optimization through simulations, although limited by the assumptions made in the model, provides insight and defines the useful parameter space.

A zero-dimensional (zero-D) (volume-averaged) optimization study for MTF systems has been reported by Jon-Erik and Scheffel [22]. That work has somewhat limited validity, since it neglects dimensionality and has not included important loss mechanisms such as thermal and magnetic flux losses from the plasma.

This work involves optimization studies for an MTF system with an inverse z-pinch target. Plasma and liner parameters are assumed to vary only in the radial (r-) direction. The study takes account of magnetic field as well as thermal diffusion, specifically of cold layer formation near the liner–plasma interface.

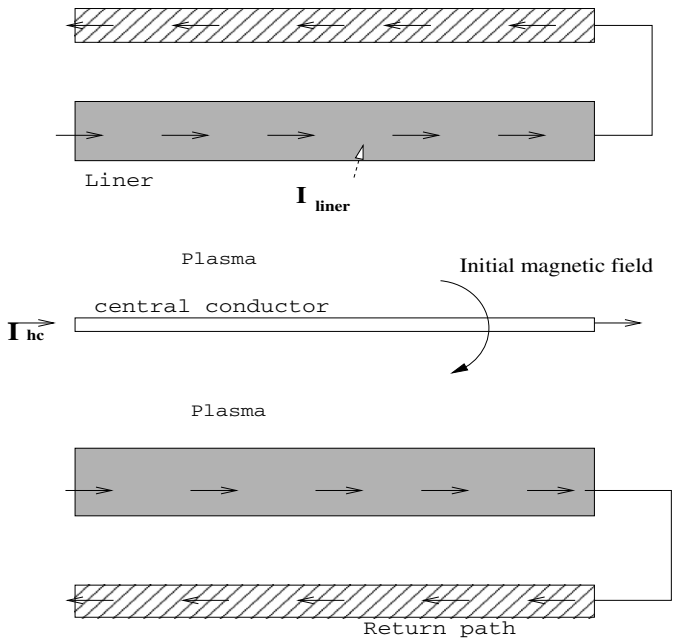

Figure 1. Schematic of the inverse z-pinch studied in this work (not to scale).

This paper is organized as follows. Section 2 provides details of the computational model. In section 3, we explain the logic of optimization and reasons for choosing the range of each parameter. Results of optimization studies are presented in section 4. In section 5, we present an energy flow analysis to better understand the optimal point. Section 6 presents results of an approximate stability analysis for one of the optimal parameter sets. Finally, section 7 lists the limitations of the model.

2. Computational model

2.1. Details of model

The general configuration of an MTF system with an inverse z-pinch target plasma is shown in figure 1.

The axisymmetric setup consists of a metallic central conductor of radius r_{hc} and a metallic outer cylindrical shell called the liner. The region in-between the liner and the central conductor contains preheated deuterium–tritium (D–T) plasma with trapped magnetic flux due to an azimuthal magnetic field B_θ. This flux corresponds to an initial current flowing through the central conductor in the axial direction. A pulsed-power source, such as a capacitor bank, drives an axial current through the liner. The return path for this current is a cylindrical shell located outside the liner. One possible electric connection is illustrated in [5]. A detailed discussion of inverse z-pinches and the dynamics of their creation can be obtained from [22].

The initial radial variation of magnetic field and density through the target plasma must be chosen such that the plasma is in MHD equilibrium and also satisfies the Kadomtsev criteria for stability against $m = 0$ and $m = 1$ modes [24]. Details of these calculations, for a specific choice of system parameters, are given in our earlier work [6], but some of the details are given below for immediate reference.

The initial MTF target plasma needs to be stable to the curvature-driven $m = 0$ (sausage) instability. This is possible if every point in the plasma satisfies the condition $Q_0 < 1$, where [24]

$$Q_0 = \frac{-(6+5\beta)}{20}\frac{r}{P}\frac{\mathrm{d}P}{\mathrm{d}r} \tag{1}$$

where the pressure P is a function of the radius r, and β is the local ratio of kinetic pressure to magnetic pressure, given by

$$\beta = \frac{2\mu_0 P}{B^2}$$

where B is the local magnetic field and μ_0 is the permeability of free space. Note that β is also a function of radial position.

For a given magnetic field distribution in space $B(r)$, the above condition implies that plasma pressure must not diminish too rapidly with increasing r.

Similarly, stability against the $m = 1$ kink mode requires $Q_1 < 1$, where [24]

$$Q_1 = -\beta\frac{r}{P}\frac{\mathrm{d}P}{\mathrm{d}r}. \tag{2}$$

Kadomtsev [24] has also shown that if the plasma is stable against the $m = 1$ mode, then it will also be stable against higher 'm' modes.

Kadomtsev has shown [24] that the condition for stability of the $m = 1$ mode is automatically satisfied if we maintain $\beta < 0.4$ and $Q_0 < 1$. Since the second condition must anyway be satisfied, we choose $\beta = 0.4$ at the outer boundary of the central conductor. Equation (2) can then be ignored for purposes of specifying the initial conditions.

Now, apart from satisfying the stability criteria, the target plasma must also be in MHD equilibrium. Hence it must satisfy the condition

$$\frac{\mathrm{d}P}{\mathrm{d}r} = -\frac{B}{\mu_0 r}\frac{\mathrm{d}(rB)}{\mathrm{d}r}. \tag{3}$$

This imposes a constraint linking $P(r)$ and $B(r)$.

Hence, given appropriate choices for Q_0 and the plasma pressure P_0 just outside the central conductor, the required $P(r)$ and $B(r)$ can be obtained by simultaneously solving equations (1) and (3).

Now, the magnetic field just outside the central conductor is given by the radius of the central conductor and the initial current flowing through it. This means that fixing β at that location (0.4 in our case) automatically fixes P_0.

Note that, in general, Q_0 and Q_1 can be functions of spatial position, so long as they remain below unity. For simplicity, in the rest of this work, we have used a constant value of Q_0 for determining initial conditions. Apart from equilibrium and stability considerations, the initial magnetic field level should be chosen so as to reduce thermal conduction losses from the plasma to the inner surface of the liner [11]. This demands a magnetic field of at least a few tesla near the liner, even at the start of liner implosion. If we assume near-adiabatic compression by the liner, the achievement of plasma temperature of a few tens of keV at peak compression requires initial temperatures of ~300–500 eV [22]. Reference [4] has reported on MHD simulations and their comparison with experiments, for the plasma creation phase in an inverse z-pinch configuration. That work reported the creation of a plasma with a temperature of 300 eV. Another simulation study [23] predicted the creation of an inverse z-pinch plasma with a temperature of 500–1000 eV. In a computational study of self-organization and the compression phase of an inverse z-pinch plasma, Siemon *et al* considered a 500 eV target plasma [5].

In this work, the one-dimensional (1D) magneto-hydrodynamic (MHD) equations are solved using a locally developed computer code. It uses an explicit, Lagrangian, finite-difference algorithm, which can handle the hydrodynamics of solids, including strength-of-material effects, as well as thermal conductivity and magnetic field diffusion.

The equations of mass and momentum continuity are given by

$$\frac{\partial \rho}{\partial t} + \frac{\partial (r\rho u)}{r\partial r} = 0 \tag{4}$$

where ρ is material density and u is the radial (R) component of velocity.

$$\frac{\partial (\rho u)}{\partial t} + \frac{1}{r}\frac{\partial (r\rho u^2)}{\partial r} + \frac{\partial P}{\partial r} + \frac{1}{r}\frac{\partial (r\sigma_r)}{\partial r} - f_r = 0. \tag{5}$$

In the above equations, P is the kinetic pressure, which is calculated using appropriate equation of state (EOS) models, explained later in this section. σ_r is the radial component of material stress, details of which are given later. For the plasma, material strength is set to zero. The body force f_r is the magnetic Lorentz force, expressed as

$$f_r = -\frac{B_\theta}{\mu_0 r}\frac{\partial (r B_\theta)}{\partial r}.$$

The energy conservation equation is given as

$$\frac{\partial}{\partial t}\left(\rho\epsilon + \frac{\rho u^2}{2}\right) + \frac{1}{r}\frac{\partial}{\partial r}\left[r\rho u\left(\epsilon + \frac{u^2}{2}\right) + rPu\right] = -\frac{1}{r}\frac{\partial (rQ)}{\partial r} - \eta J^2 + E_{\mathrm{f}} \tag{6}$$

where ϵ is the internal energy density, η is the electrical resistivity of the medium and J is the current density. $Q = -\kappa \partial T/\partial r$ is the thermal flux and κ is the thermal conductivity.

E_{f} is the energy released during fusion reactions in the form of kinetic energy of charged particles, which is assumed to be deposited locally. Finally, the magnetic field is updated using the diffusion equation:

$$\frac{\partial B}{\partial t} = \frac{\partial}{\partial r}\left[\frac{\eta}{\mu_0 r}\frac{\partial (rB)}{\partial r}\right] - \frac{\partial (uB)}{\partial r}. \tag{7}$$

Hence the three conservation equations for mass, momentum and energy, along with the magnetic field diffusion equation, are evolved in one space coordinate (r) and time, under the assumption of axisymmetry and axial uniformity. The outer boundary of the computation region is assumed to lie at the outer surface of the liner.

It should be noted that the magnetic field is assumed to have only an azimuthal component. In general, an inverse z-pinch plasma may have an additional axial component as well. This axial component can have a stabilizing effect on inverse z-pinch plasmas [4, 18]. However, the axial component cannot be included in the 1D study performed in this work.

We have earlier used the same model for the study of cold layer formation in inverse z-pinch MTF systems, albeit with an approximate EOS for aluminum. Details are available from [20]. However, some important features of the model are summarized below for the sake of completeness.

- The Steinberg–Guinan rate-independent expression has been used for calculating the dependence of yield strength [25] and shear modulus of the aluminum (Al) liner on the temperature, pressure and plastic strain.
- The ideal gas EOS is used for plasma, assuming full ionization.
- Bremsstrahlung losses from the plasma are taken into account, but reabsorption of the radiation in the liner is not taken into account.
- The magnetic field diffusion equation is solved using the implicit Crank–Nicholson method [26].

- The Burgess electrical resistivity model for multi-phase systems [27] has been used for the aluminum liner. An overview of the model is given below for the sake of completeness. This is a semi-empirical model, covering the entire range of densities and temperatures spanning solid, liquid, vapor and plasma phases. It provides smooth interpolation in resistivity between different phases. The resistivity is calculated as a function of temperature and specific volume.

  In the solid state, resistivity is given by

$$\eta_s = \left(C_1 + C_2 T^{C_3}\right) f\left(\frac{V}{V_0}\right) \tag{8}$$

where C_j are material-dependent coefficients [27], V is the specific volume and V_0 is the specific volume under standard conditions and T is the temperature.

Liquid phase resistivity η_l is given by

$$\eta_l = (\eta_l)_{\mathrm{m}} \left(\frac{T}{T_{\mathrm{melt}}}\right)^{C_4} \tag{9}$$

$$(\eta_l)_{\mathrm{m}} = \Delta\eta(\eta_s)_{\mathrm{m}} \tag{10}$$

where subscript 'm' refers to the quantity evaluated at the melting point, and

$$\Delta\eta = k\mathrm{e}^{80L_{\mathrm{f}}/T_{\mathrm{m}}}$$

where L_{f} is the latent heat of fusion (kJ mole^{-1}) and T_{m} is the melting temperature (K).

The vapor phase and plasma phase resistivity includes contributions from electron–ion and electron–neutral collisions, and is given by

$$\eta_{\mathrm{ei}} = \frac{C_5}{T}\left[1 + \ln(1 + C_6 V T^{3/2})\right] \tag{11}$$

$$\eta_{\mathrm{en}} = C_7 T^{1/2}(\delta_{\mathrm{i}}^{-1} + 1) \tag{12}$$

where δ_{i} is the degree of ionization, given by

$$\delta_{\mathrm{i}} = \left(1 + \frac{c_8 \mathrm{e}^{C_9/T}}{V T^{3/2}}\right)^{-1/2}.$$

In the case of mixed phases, consisting of a combination of vapor and condensed phases, a mixing parameter can be defined as

$$m = (V - V_0)\frac{C_{10}}{C_{11}}\mathrm{e}^{C_{12}/\theta} \tag{13}$$

where 'm' is the mass fraction of material in the vapor phase. Two mixing constants are defined:

$$X_c = (1 - m)(V/V_0) \tag{14}$$

$$X_v = 1 - X_c \tag{15}$$

and the mixed-phase resistivity is given as

$$\eta_{\mathrm{mix}} = \left(\frac{X_c}{\eta_c} + \frac{X_v}{\eta_v}\right). \tag{16}$$

Since the target plasma is fully ionized, the Spitzer resistivity is used, given by

$$\eta = 1.30 \times 10^2 \frac{Z \ln\lambda}{T^{3/2}} \tag{17}$$

where T is the temperature (K), Z is the average charge state and $\ln\lambda$ is the Coulomb logarithm.

- Bohm thermal diffusion coefficients are used for thermal transport in the plasma [28]. This is likely to overestimate transport losses from the plasma to the liner [11], yielding a conservative result for fusion yield.
- Detailed 1D results from the MHD model are used to generate macroscopic electrical properties of the system as functions of time, i.e. the inductance L_f, resistance R_f and the rate of change of inductance dL_f/dt. These parameters, evaluated at each time step, are then used to update a circuit solver to self-consistently obtain the circuit current as a function of time.
- Four fusion reactions are taken into account:

$$D_1^2 + T_1^3 \rightarrow He_2^4(3.50\,\text{MeV}) + n_0^1(14.1\,\text{MeV}) \tag{18}$$

$$D_1^2 + D_1^2 \rightarrow He_2^3(0.82\,\text{MeV}) + n_0^1(2.45\,\text{MeV}) \tag{19}$$

$$D_1^2 + D_1^2 \rightarrow T_1^3(1.01\text{MeV}) + p_1^1\ (3.02\,\text{MeV}) \tag{20}$$

$$D_1^2 + He_2^3 \rightarrow He_2^4\ (3.66\,\text{MeV}) + p_1^1\ (14.7\,\text{MeV}). \tag{21}$$

  Changes in plasma composition with time due to these reactions are also taken into account. Charged particles produced in these reactions, e.g. alpha particles, are assumed to deposit their energy locally.

Because of the large conduction heat flux from the bulk (hydrogen) plasma to the liner, the temperature of the liner inner surface is expected to become high enough to produce a dense aluminum plasma. To handle this, we have included an EOS for the aluminum liner which is valid over the entire range of densities and temperatures expected in this system, including dense plasma [29]. For lower temperatures, we have used an EOS as described in [30] and implemented in [29]. For high-temperature, low-density plasmas, we have used an EOS based on the IONMIX code [31].

At this point it should be noted that both Ettingshausen and Nernst effects are ignored in this study. A justification for the same is given below. Vekhtein has previously reported the effect of the Nernst term on magnetic diffusion in [12, 32]. The Nernst term in the magnetic diffusion equation will additionally drift the field lines toward the cold boundary (liner). From the references, it is also clear that this effect becomes important only for plasmas with $\beta \gg 1$. Figure 2 shows a typical temporal variation of β at different locations in the system, as yielded by the simulations covered in this work. We observe that, for the parameter range examined in this study, plasma β is less than unity except toward the end of the burn phase. Even at those times, it is only in the bulk plasma that β exceeds unity. However, in the burn phase, fusion energy deposition time scales would be much shorter than time scales for energy leakage by any process, leading to near-adiabatic heating. Hence neglect of the Nernst effect is justified.

The Ettingshausen effect tends to enhance thermal losses toward the cold wall, which amounts to increasing the thermal conductivity. Reference [32] has shown that classical thermal conductivity is enhanced by the Ettinghausen effect to a value of the order of the Bohm value. Since we are anyway using the Bohm value in our calculations, inclusion of the effect would not change the results.

2.2. Comparison of model with earlier zero-D model

In this subsection, we will explain the key differences between this study and a volume-averaged (zero-D) study reported in [22].

(i) The zero-D model used for optimization in [22] evolves volume-averaged quantities. This means that radial or axial variations of quantities such as density, temperature and magnetic fields are neglected. The decelerating pressure (sum of kinetic and magnetic

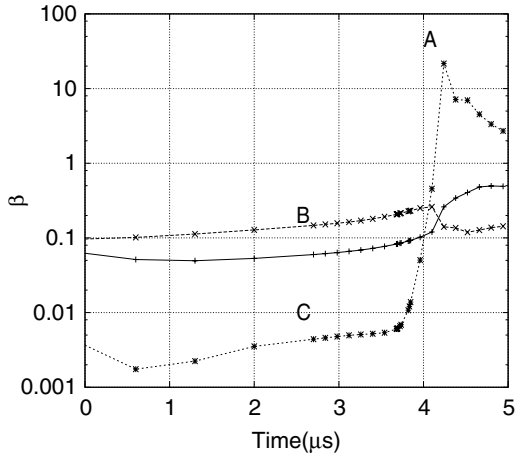

Figure 2. Temporal evolution of plasma β at three radial locations in the plasma: (A) near the liner, (B) at the boundary of the cold layer and bulk plasma, (C) in the bulk plasma.

pressure) 'seen' by the liner for that case would be the volume-averaged pressure. The actual pressure seen by the liner could be significantly different from the average pressure, especially due to cold layer formation, for two reasons. Firstly, the cold layer immediately adjacent to the liner has a lower pressure than the average, Secondly, at least in the case of an inverse z-pinch target, radially decreasing density and magnetic field profiles are required due to stability requirements. This also means that the pressure near the liner would be lower than the average. Both these effects may lead to higher implosion velocities and/or higher peak compressions than those yielded by the zero-D case.

(ii) The zero-D model does not include thermal energy loss from the plasma to the liner due to high-temperature gradients between liner and plasma. In the same way, magnetic diffusion is also neglected. The present model includes both these effects.

(iii) The zero-D model has been applied to an FRC target while we have considered an inverse z-pinch target. The magnetic field profiles and density profiles are considerably different in the two concepts.

3. Optimization procedure

The goal of the optimization process is to obtain maximum output fusion energy for a given initial energy in the capacitor bank. Table 1 shows the parameters that are held constant throughout the optimization. Capacitor bank parameters are based on those of Atlas [5]. It should be noted that the resistance mentioned in the table is not the total resistance of the system. Rather, it is the resistance of conductors connecting the capacitor bank to the system, joints, etc. Hence we have assumed a fixed value. The self-consistent resistance of the plasma–liner system is actually calculated as a function of time and used in the model.

The energy gain is defined as the fusion energy output divided by the initial energy in the capacitor bank.

The D–T target plasma, comprising equal amounts of D and T, is assumed to have a uniform initial temperature of 500 eV unless otherwise specified. The liner is assumed to start from rest at $t = 0$. An inverse z-pinch target plasma is considered in this study. The initial pressure and magnetic field profiles in the plasma are chosen so as to satisfy the Kadomtsev

Table 1. Parameters of system studied.

Central conductor radius	5 mm
Charging voltage of capacitor bank	480 kV
Stored energy in bank	35 MJ
Bank capacitance	0.31 mF
Total resistance of system excluding plasma and liner (assumed)	1.0 mΩ
Initial radial gap between current return path and liner outer radius	0.5 cm
Initial Kadomtsev stability parameter Q_0	0.9
Maximum value of plasma β	0.4

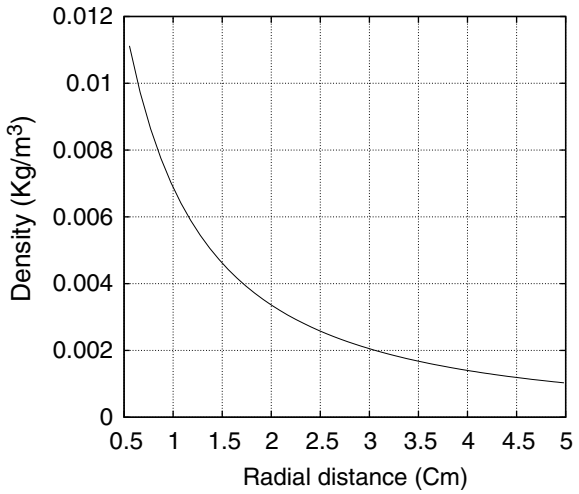

Figure 3. Radial profile of initial density for case b of table 3.

stability criteria, as detailed in section 2. The value of the Kadomtsev stability parameter Q_0 is chosen as 0.9 and maximum plasma β at 0.4. This choice of pressure and temperature profiles yields initial density profiles of the type shown in figure 3, which corresponds to case b of table 3.

The following parameters have been varied during optimization:

(i) Initial magnetizing current (I_M).
(ii) Initial liner length (l_0).
(iii) Initial liner radius (R_0).
(iv) Initial liner thickness (dR).

The reasons for choosing these parameters are explained below.

3.1. Initial magnetizing current (I_M)

The initial magnetizing current plays two conflicting roles in an MTF system. On the one hand, increasing the initial magnetic field reduces thermal transport losses from the plasma. The thermal diffusivity scales as B^{-2} and B^{-1} for classical and Bohm diffusion, respectively. Lower thermal losses lead to higher plasma temperatures, thereby increasing the fusion yield. On the other hand, the liner pushes against not just the thermal pressure of the plasma, but also the magnetic pressure associated with the magnetizing field. Hence a higher initial field leads to higher liner deceleration, reducing peak compression. An example will illustrate the point,

Table 2. Parametric space used in this study.

Parameter	Minimum	Maximum	Number of points
Initial magnetizing current	0.5 MA	2.5 MA	4
Liner length	7 cm	30 cm	3
Initial liner radius	3 cm	5 cm	3
Initial liner thickness	1 mm	4 mm	3

for the parameters: $I_M = 1.5$ MA, $l_0 = 30$ cm, $R_0 = 5.0$ cm and $dR = 1$ mm. For this case, our simulations show that 22 MJ of energy is delivered by the liner, out of which 14 MJ is used to compress the magnetic field. Only 3 MJ is converted to plasma thermal energy. Hence only a small fraction of stored capacitor bank energy is used for heating the plasma.

3.2. Liner length (l_0)

Increasing the liner length also produces several conflicting effects. Higher length increases plasma volume and hence 'fuel' availability for fusion. It also reduces the relative importance of thermal losses through the 'side walls', albeit at the cost of higher surface area of the liner.

Higher length also increases circuit inductance. This reduces the peak current and hence the peak magnetic pressure driving implosion, which is harmful. On the other hand, it increases the width (duration) of the current pulse, which means that the magnetic pressure, although somewhat smaller, acts for a longer time, which is beneficial. However, a longer compression time also allows more time for growth of instabilities.

3.3. Initial liner radius (R_0)

An increase in initial liner radius allows more space for fuel, which is beneficial. However, it increases the surface area for thermal losses and impurity generation by plasma–surface interaction, both radially and at the side walls, which is harmful. Higher initial radius also implies higher compression time, allowing more time for instability growth. On the other hand, the higher liner mass and hence inertia would allow longer dwell time at peak compression, increasing the fusion yield.

3.4. Initial liner thickness (dR)

Higher initial liner thickness will increase liner mass, causing two conflicting effects. Firstly, for given capacitor bank parameters, liner acceleration would be smaller, reducing liner implosion velocities and peak compression. However, the larger inertia would increase dwell time, improving energy output.

The above discussion shows that a systematic self-consistent study is required to determine the optimal operating point.

3.5. Parameter space

The parameter space examined in this study is defined in table 2.

The range of initial magnetizing current has been selected as follows. We start with the assumption that a magnetizing field of a few tesla is essential at the inner surface of the liner. Taking a nominal liner radius of 5 cm, we get a minimum magnetizing current of 0.5 million amperes (MA). The upper limit on I_M has been determined as follows. Holding the

Table 3. Parameter sets yielding an energy gain exceeding unity.

	I_M (MA)	R_0 (cm)	l_0 (cm)	dR (mm)	Energy gain
a	0.5	5	10	1	1.11
b	0.5	5	10	2	3.94
c	0.5	5	7	2	2.74
d	0.5	5	10	4	1.10
e	0.8	5	10	1	1.00
f	0.8	5	10	2	2.27
g	0.8	5	7	2	1.06

other parameters constant at d$R = 1$ mm, $l_0 = 10$ cm and $R_0 = 5$ cm, simulations have been performed with progressively increasing I_M until the energy gain starts falling off. Finally, four values have been selected in the range 0.5–2.5 MA.

The procedure for choosing the ranges of liner length and liner initial radius is explained below. Ideally in 1D simulations like this, one should keep liner length greater than liner diameter to avoid two-dimensional (2D) effects. We performed trial simulations by varying only liner length and radius, keeping other parameters constant with values of d$R = 1$ mm, $I_M = 1.5$ MA. In these trials, the liner radius is varied from 3 to 6 cm and length from 7 to 30 cm. The maximum gain is obtained around 10 cm liner length. Hence, in order to avoid 2D effects, and to have a consistent parametric set, we fixed an upper bound for the liner radius at 5 cm, half of the possible optimum liner length. From the same trial runs, the lower bound for liner radius is fixed at 3 cm and upper bound for liner length at 30 cm.

The values for liner length chosen are 7, 10 and 30 cm and the radius values are 3, 4 and 5 cm.

The minimum initial liner thickness has been taken as 1 mm, since smaller thicknesses would be difficult to handle in practice and also may not be able to carry the large currents. The other values are 2 and 4 mm.

Hence the optimization involves a total of $4 \times 3 \times 3 \times 3 = 108$ computational runs.

4. Results and discussion

The results of this study are subject to some important limitations which are listed in section 7. The objective of this work is limited to determining a parameter range which yields the highest gain, which can serve as a focus for more detailed investigations.

4.1. Optimum set and energy gain

Out of the 108 parametric sets scanned, 7 sets are found to yield an energy gain exceeding unity. These are summarized in table 3.

Table 3 shows that increasing magnetizing current reduces the gain, the best results coming at $I_M = 0.5$ MA. Since this is the lower limit in the study, it is necessary to check if a further reduction in I_M would be beneficial. Hence simulations have been repeated for the first four parameter sets in table 3, with $I_M = 0.4$ MA. The gain is found to be lower than the corresponding cases with 0.5 MA.

An initial liner radius of 5 cm gives the maximum gain in all cases. In any case, higher values of R_0/l_0 would imply that 2D effects would become progressively more important, Hence the 1D study performed here would become progressively inaccurate.

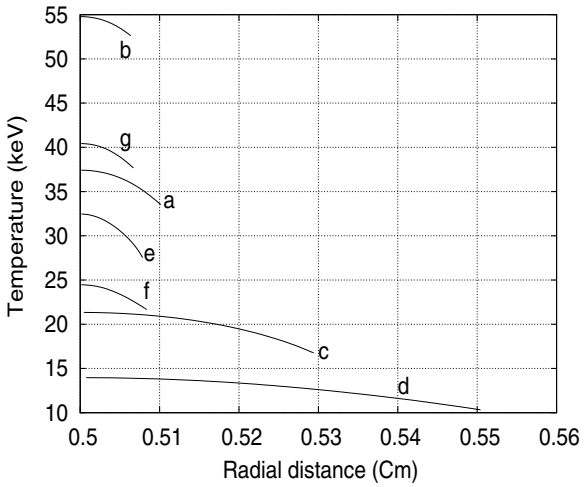

Figure 4. Radial profiles of plasma temperature during the burn phase for the cases having a gain exceeding unity. Labels (*a*)–(*g*) are in accordance with the numbering in table 3.

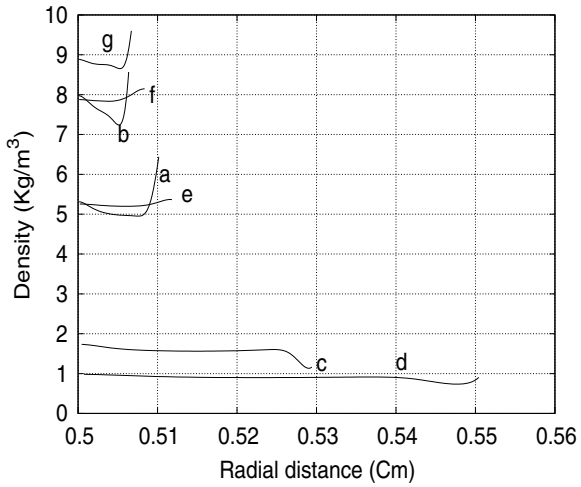

Figure 5. Radial profiles of plasma density during the burn phase for the cases with a gain more than unity. Labels (*a*)–(*g*) are in accordance with the numbering in table 3.

Increasing the liner length from 7 to 10 cm gives higher gain, but any further increase reduces the gain. The same trend is observed with initial liner thickness. Cases with liner thickness of 2 mm are found to give higher gain in all cases considered.

Figures 4, 5 and 6 show radial profiles of temperature, density and magnetic field through the plasma around the time of peak compression (burn phase). The results are presented for all the seven cases where the gain is more than unity. The results show a high level of plasma compression. The radial extent of the plasma, between the inner surface of the liner and the outer surface of the central conductor, varies between 64 μm and 0.5 mm. In reality, such a high level of compression may be limited by axial and azimuthal instabilities. Since this study permits only radial variations, those instabilities will not appear in the results. 2D and

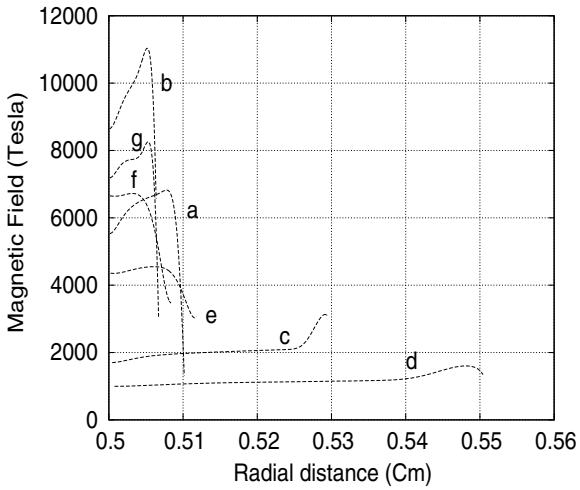

Figure 6. Radial profiles of magnetic field in the plasma during the burn phase, for cases with a gain exceeding unity. Labels (*a*)–(*g*) are in accordance with the numbering in table 3.

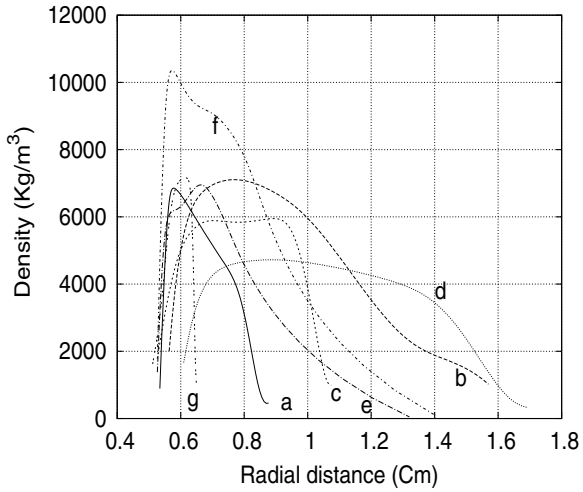

Figure 7. The radial profile of liner density in burn phase for the cases with a gain more than unity. Labels (*a*)–(*g*) are in accordance with table 3.

three-dimensional (3D) studies are required to probe to what extent the instabilities limit the convergence. However, as discussed earlier, we have chosen the initial parameter space such as to exclude regimes where 2D effects are obviously important. Furthermore, in section 6, an approximate liner stability study will be performed to examine which modes are likely to go unstable. The objective of this study is to identify useful regimes that can be examined in a more detailed 2D and 3D study.

Figure 7 shows the radial profile of liner density through the liner thickness, at the same times as in figure 5.

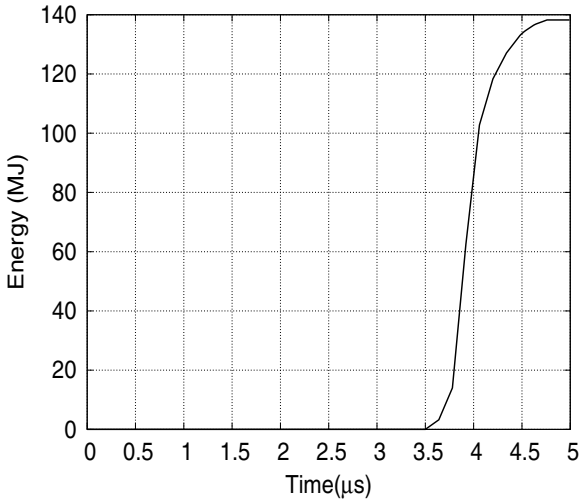

Figure 8. Temporal variation of cumulative energy output.

4.2. Details for the case with maximum gain

In this subsection, we present detailed results for the case with maximum gain. The corresponding parameter set is $I_{\mathrm{M}} = 0.5\,\mathrm{MA}$, $l_0 = 10\,\mathrm{cm}$, $R_0 = 5\,\mathrm{cm}$ and $\mathrm{d}R = 2\,\mathrm{mm}$, which yields an energy gain $\simeq 4$.

Figure 8 shows the time-integrated energy output as a function of time. The energy output during the compression phase, up to $3.5\,\mu\mathrm{s}$, is negligible, and the output saturates around $4.75\,\mu\mathrm{s}$. Hence the burn phase lasts for just over $1\,\mu\mathrm{s}$.

Figure 9 compares the cumulative energy deposition by fusion-produced charged particles with the cumulative energy loss by thermal diffusion into the liner. It clear that during the burn phase, fusion energy deposition rate is higher than the thermal loss rate, which is why the plasma bootstraps itself to higher temperatures.

Figure 4 shows the radial profile of plasma temperature during the burn phase, at $t = 4.60\,\mu\mathrm{s}$, the time corresponding to peak temperatures in the plasma. The spread in plasma temperatures is small. This means that the temperature gradient through the cold layer is not significant at this time. This can be understood as follows. A spread in plasma temperature is mainly caused by thermal loss from plasma to liner. Because of thermal transport from plasma to liner, temperatures near the liner will tend to be lower than the bulk plasma temperature. However, during the burn phase, the rate of fusion energy deposition is higher than the thermal loss rate. Hence the entire plasma gets heated up to a nearly uniform temperature.

Figure 10 shows the time-integrated neutron output as a function of time. In the same figure we have also shown the temporal evolution of total number of ${}_2\mathrm{He}^4$. This shows that, although four fusion reactions are included, the D–T reaction is dominant.

Figure 11 shows the temporal evolution of the remaining number of deuterium ions as a fraction of the initial number. The peak burnup is 24%.

5. Analysis of energy flow

In section 3, we had listed the conflicting effects on energy gain produced by varying system parameters. It is desirable to understand, quantitatively, how these effects work together to

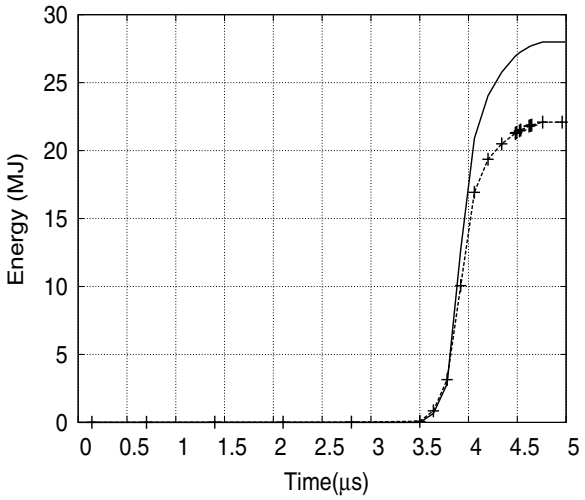

Figure 9. A comparison of time-integrated thermal energy loss to liner (line with symbols) and time-integrated energy deposited by charged particles (line) as a function of time.

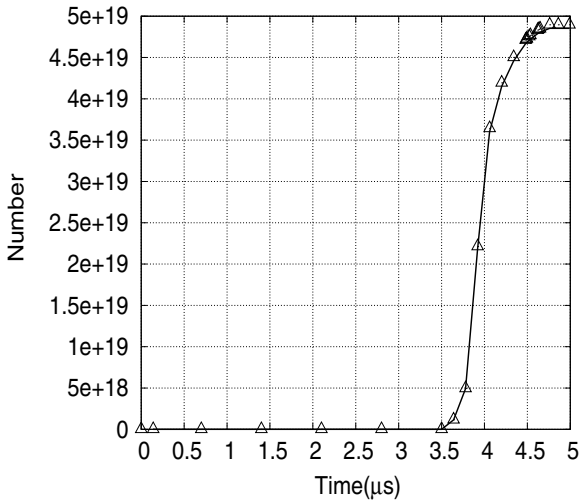

Figure 10. Temporal variation of total neutron number (symbols) and $_2He^4$ number (line).

make a certain parameter set 'optimal'. This is done in this section using an analysis of energy flows.

We have performed another set of simulations, varying only one parameter at a time around the optimal point, and keeping the other parameters constant. For example, the initial magnetizing current has an optimal point at $I_M = 0.5$ MA. Hence, in the new runs, we vary I_M from 0.4 MA to 0.6 MA, keeping all other parameters at their optimal values. For each such value, we determine various energy flows into and out of the system. The primary energy sources are the energy delivered from the capacitor bank and energy deposited by fusion-produced charged particles. This source energy can then be converted to other forms through Joule heating in the entire system, compressing plasma (increasing internal energy

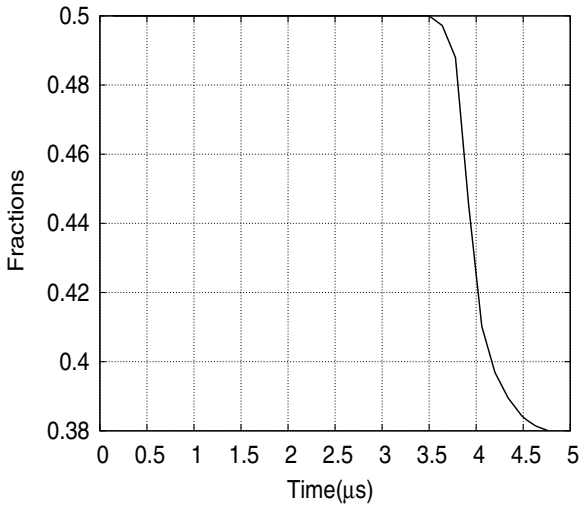

Figure 11. Fraction of initial deuterium still remaining in the plasma. The peak burnup can be seen to be 24%.

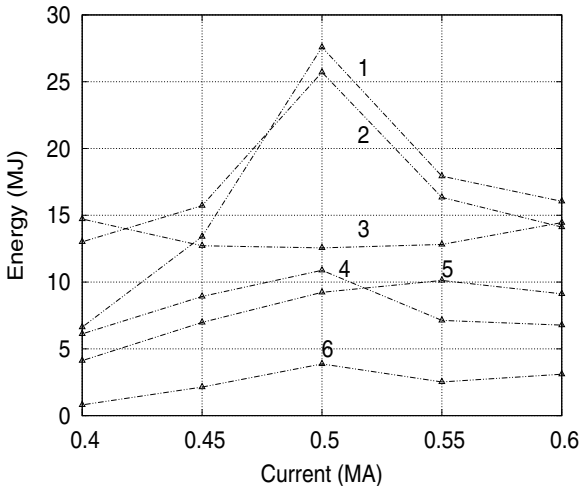

Figure 12. Energy flow for different values of the magnetizing current. (1) Energy deposition by charged particles. (2) Thermal energy loss to liner. (3) Joule heating. (4) Plasma internal energy. (5) Plasma magnetic energy. (6) Magnetic energy loss.

of the plasma), compressing the magnetic field, thermal loss from the plasma to the liner and magnetic energy loss from plasma to the liner. These contributions are then analyzed to obtain physical insight about the optimal points. In all cases, the analysis is performed at time points lying toward the end of the burn phase.

5.1. Initial magnetizing current (I_M)

Figure 12 shows various energy terms at the end of the burn phase. For example, curve 2 is the total thermal energy leakage into the liner from $t = 0$ upto the end of the burn phase.

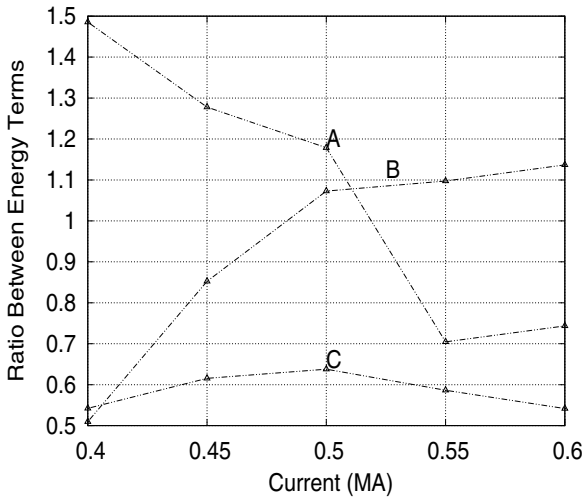

Figure 13. Ratio of various energy terms. (A) Ratio of internal energy to magnetic energy. (B) Ratio of charged particle heating to thermal energy loss. (C) $1 - E_{\text{Joule}}/E_{\text{c}}$.

Figure 13 shows the ratios between various source and sink terms. E_{Joule} is the energy dissipated through Joule heating in the system and E_{c} is the initial energy in the capacitor bank. Hence $1 - E_{\text{Joule}}/E_{\text{c}}$ is the total energy that is converted to useful work in the system, e.g. kinetic energy of the liner and compression of the magnetic field.

For lower values of I_{M}, the internal energy is high as compared with the magnetic energy. However, the thermal loss rates are much higher than the rate of heat deposition by charged particle heating. This is because low I_{M} corresponds to less magnetization, yielding higher thermal leakage. Higher I_{M} improves magnetic insulation. However, it also implies higher magnetic fields on the inner surface of the liner, so that a larger fraction of the liner kinetic energy is used in doing work against magnetic pressure. The net result of higher I_{M} is, therefore, a reduction in compression and hence in the fusion yield. Figure 13 also shows that the optimum point exists at $I_{\text{M}} = 0.5$ MA. Curve (C) shows that a larger fraction of the stored capacitor energy is converted to useful work around the optimum point even through the variation with I_{M} is not too large.

5.2. Liner length

Figure 14 shows various energy ratios as functions of liner length. The ratio of internal energy to magnetic energy does not change significantly with 'l', and both terms are approximately comparable. The same is true of the ratio of charged particle energy deposition to thermal energy loss. This insensitivity is due to our neglect of end-losses. In real life, the end losses would tend to increase for smaller liner lengths.

5.3. Liner initial thickness

Figure 15 shows the ratio between various energy terms. The ratio of plasma internal energy to magnetic energy is relatively insensitive to liner thickness. However, curve (B) shows that the ratio of charged particle energy deposition to thermal leakage is a very sensitive function of thickness, varying between 0.63 and 1.08. This can be understood as follows. Lower

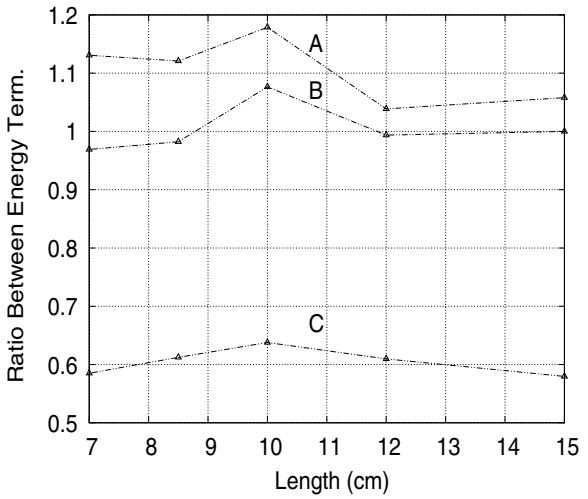

Figure 14. Ratio of various energy terms around optimal liner length $l = 10$ cm (A) Ratio of the internal energy to magnetic energy. (B) Ratio of charged particle heating to thermal energy loss. (C) $1 - E_{\text{Joule}}/E_{\text{c}}$.

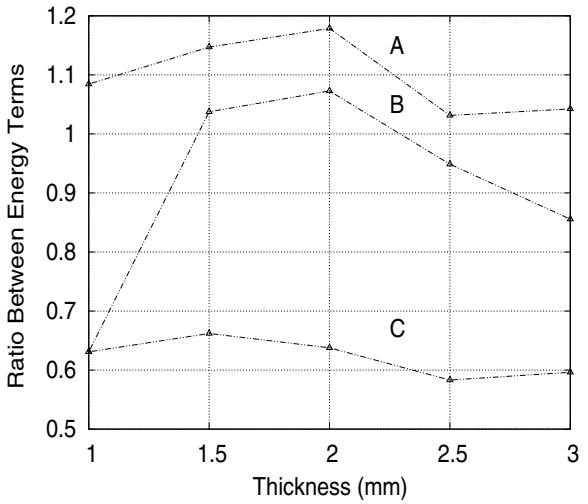

Figure 15. Ratio of various energy terms around the optimal initial liner thickness of 2 mm. (A) Ratio of the internal energy to magnetic energy. (B) Ratio of charged particle heating to thermal energy loss. (C) $1 - E_{\text{Joule}}/E_{\text{c}}$.

liner thickness results in higher implosion velocities which, in turn, produces higher peak compression and plasma temperature. That, in turn, leads to higher fusion power levels and hence the power deposition by charged particles. However, due to the lower liner mass, the tamping effect is reduced, leading to a smaller burn time. For a given fusion power level, smaller burn time tends to reduce the total fusion energy output and hence the total energy deposition by charged particles. Similarly, for a given thermal leakage rate, lower burn time reduce the total thermal leakage. Given the different scaling of fusion power density and thermal leakage rate with plasma temperature, it is reasonable to expect an optimal liner thickness.

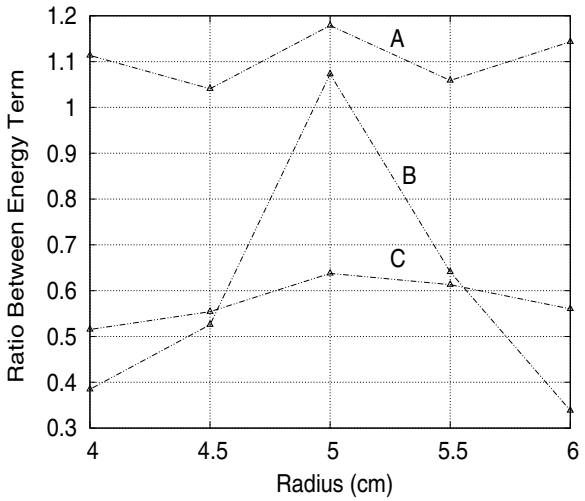

Figure 16. Ratio of various energy terms around optimal initial liner radius $R_0 = 5$ cm. (A) Ratio of the internal energy to magnetic energy. (B) Ratio of charged particle heating to thermal energy loss. (C) $1 - E_{\text{Joule}}/E_{\text{c}}$.

5.4. Liner initial radius

From figure 16, curve (A), it is clear that the ratio between the plasma internal energy and magnetic energy is insensitive to the initial liner radius. Hence it does not play a major role in determining the optimal point. However, curve (B) shows large variation. This can be understood as follows. Let us start with an initial radius of 4 cm. The total 'fuel' available for fusion increases as the square of this radius. Hence, assuming that the plasma gets compressed to similar peak densities and temperatures, we would expect higher fusion yields and hence energetic particle deposition as the initial radius increases. However, as the radius increases, the implosion time also increases, not only because of the longer distance to be traveled but also due to the $1/r$ variation of magnetic field acting on the outer surface of the liner. This allows more time for thermal energy leakage. For example, the time to peak compression is 3.5 μs, 5.5 μs and 6 μs for $R_0 = 5$ cm, 6 cm and 7 cm, respectively. In addition, the inner surface area of the liner also becomes higher. The net effect is higher total thermal leakage. The conflicting effects of more fusion fuel and higher thermal losses implies an optimal point in liner radius.

6. Role of instabilities

The above results have been obtained from a 1D study. One of the major assumptions is the neglect of liner instabilities, which would only show up in a 2D or 3D study. The growth of instabilities, either in the liner or in the plasma, is likely to degrade system performance, since they would lead to mixing of ablated liner material with the plasma and mixing of hot and cold plasma.

The role of magnetic Rayleigh–Taylor instabilities in MTF systems with an inverse z-pinch target plasma has been studied in [33]. 2D MHD simulations were compared with analytical expressions [34] for the critical wavelength and critical amplitude for the growth of such instabilities in solid liners with material strength. In this section, we attempt to define limits

on liner roughness such that these instabilities are not a problem for the optimal system configuration determined in the last section. The results of this work are more likely to be correct if these limits on roughness are satisfied in the experimental system, so that instabilities are not an issue up to the point of peak compression.

Equations (22) and (23), derived in [34], define limits on unstable wavelength modes and on critical amplitudes. All wavelengths greater than those defined by equation (22) are expected to become unstable. Even if a wavelength is stable based on the wavelength criterion, it can become unstable if the amplitude of the perturbation crosses the amplitude limit defined by equation (23). Note that the critical amplitude condition is valid only if $\lambda < \lambda_{\mathrm{cri}}$. More details, including the methodology of derivation of equations (22) and (23), can be obtained from [34].

$$\lambda_{\mathrm{cri}} = \frac{4\pi C^2}{a}\left[1 - \exp\left[-\frac{2\pi H}{\sqrt{3}\lambda_{\mathrm{cri}}}\right]\right] \tag{22}$$

$$\delta H = \frac{Y(kH)^2}{6\sqrt{3}\rho a}\left[1 - \left(\frac{k_{\mathrm{cri}}}{k}\right)^4\right] \tag{23}$$

where Y is the yield strength, $k = 2\pi/\lambda$ is the wave-vector, $k_{\mathrm{cri}} = 2\pi/\lambda_{\mathrm{cri}}$, H is the thickness of the liner, 'a' is the liner acceleration and $C = (G/\rho)^{\frac{1}{2}}$, where G is the shear modulus of the metal and ρ is its density.

Equation (22) is implicit in λ_{cri} and has been solved numerically using a root finding algorithm.

These expressions can be used to evaluate the time-dependent critical wavelength for both inner and outer surfaces of the liner, using time-varying Y, G and acceleration yielded by the 1D MHD simulation. We have separately examined inner and outer surfaces of the liner since these quantities would, in general, be different for the two surfaces. It should also be noted that the liner would lose its strength gradually due to the radiative and conductive heat flux from the plasma, as well as due to Joule heating. The strength would fall to zero when the corresponding surface melts.

Once the critical wavelength is calculated using equation (22), it can be used for critical amplitude calculations using equation (23). Now, during liner fabrication, it is possible to control the surface roughness, and hence the amplitude of perturbations. However, it may not be easy to maintain control over the wavelengths of the perturbations. Hence, to ensure liner stability, one should ideally keep the surface roughness below the critical amplitude of all wavelengths that could arise in the liner.

It must be emphasized that this calculation is valid only up to the point where the liner melts. Further instability growth will be similar to that of a fluid without strength.

Figure 17 shows the temporal evolution of critical wavelength for both inner and outer surfaces, for the case with maximum gain.

Recalling equation (22), the critical wavelength decreases with increasing acceleration at early times. As time goes on, the strength decreases and acceleration also decreases, leading to a minimum in the critical wavelength. The minimum values for the inner and outer surface are 0.5 cm and 1.5 cm, respectively. This calculation has been done only up to the point where the corresponding surface melts. The inner surface receives a large thermal flux from the plasma. The consequent rise in temperature reduces material strength. This explains why, after a startup period, the inner surface has a lower value of critical wavelength as compared with the outer surface.

We next calculate the critical amplitude for the system for maximum gain. Now, this is a function of wavelength, and tends to decrease with increasing wavelength. Hence it

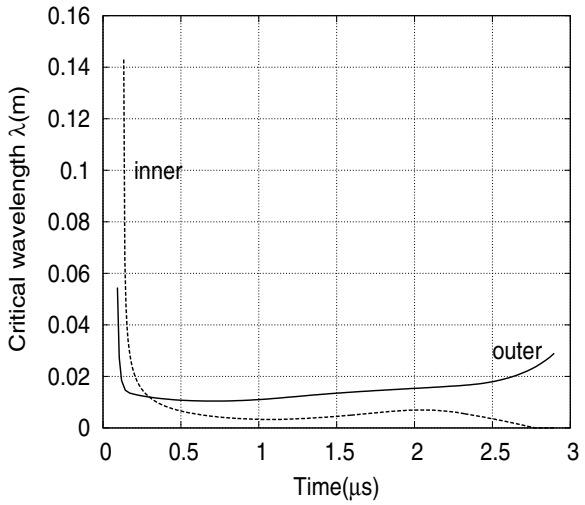

Figure 17. Temporal variation of critical wavelength for the system exhibiting maximum energy gain.

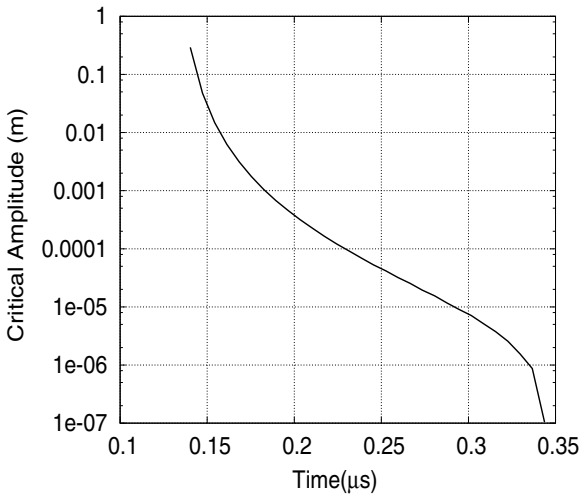

Figure 18. Temporal variation of critical amplitude on the inner surface of the liner, corresponding to a wavelength equal to length of the system, for the system with maximum gain.

has been calculated for the longest wavelength that can arise in this system, namely, 10 cm, corresponding to liner length.

Figure 17 shows that for the outer surface, the critical wavelength is smaller than the system length from fairly early times. This is because the outer surface experiences the magnetic pressure well before the inner surface experiences it. Hence it is not meaningful to calculate the critical amplitude for the outer surface—it is potentially unstable from fairly early times. The inner surface is stable, based on the wavelength criterion, up to 0.35 μs—hence the critical amplitudes can be calculated up to this time point, and is shown in figure 18.

7. Limitations of this model

(i) 2D effects have been ignored. This means that liner and plasma instabilities are not taken into account, which is why a highly simplified stability study has been performed. Since we have made use of 1D simulations, all axial gradients are ignored. Similarly, thermal conduction losses to the side walls (glide planes) of the liner have been neglected.

(ii) Physical mixing of the liner material with the fusion plasma has been neglected. Ablation/sputtering of the liner due to the high heat flux on its inner surface will lead to mixing of liner material with the plasma. This, in turn, will enhance impurity radiation from the plasma, leading to enhanced cooling.

(iii) We have used a highly simplified model for radiation transport in the entire system. Bremsstrahlung losses from the plasma have been taken into account, but without including reabsorption in the liner. Radiation emission and absorption within the liner has also not been taken into account.

(iv) Neutral particle dynamics has been ignored. However, note that the target plasma is assumed to start at a temperature of 500 eV and is further compressed and heated. Hence the dynamics of hydrogen neutrals may not be very important, except in a thin boundary layer near solid surfaces.

(v) Capacitor bank parameters have not been optimized—it could happen that for the same total energy, a different set of capacitor bank parameters may yield better results.

(vi) This work assumes local alpha particle energy deposition. This makes this work optimistic in terms of energy gain. A small discussion of this point is given below.
The minimum radial extent of the plasma, around peak compression, is $\sim$1 mm. The Larmor radius at that time is calculated as $\sim$100 μm, which indicates that alpha particles produced in the outer plasma region near the liner could escape from the plasma. But this outer part is partially occupied by a low-temperature cold layer, which is not expected to contribute significantly to fusion output and alpha production. This means that the assumption may not lead to very large errors.

8. Conclusions

We have performed an optimization study for an inverse z-pinch MTF system, with the aim of maximizing fusion energy output by varying quantities such as the magnetizing current, the liner radius and thickness and liner length. All other system parameters, including capacitor bank parameters, are held constant. The initial target plasma is taken to have plasma profiles close to the Kadomtsev stability limit. The plasma–liner system is treated using a one-dimensional MHD model, including the effect of dynamic material strength in the liner.

The optimization study has yielded several parameter sets that have an energy gain exceeding unity, i.e. where the fusion energy output exceeds the initial capacitor bank energy.

During the burn phase, the thermal loss rate is lower than the heating rate by charged particle slowing down. This leads to a fairly 'flat' temperature profile in the plasma.

An energy flow analysis has been carried out in order to understand the physical process which determine the optimal point.

In an experimental system, the reduction in liner strength due to heating, and complete loss of strength due to melting, would lead to growth of instabilities. That would further degrade performance. For the case with highest energy gain, a simple liner stability analysis has been performed. This involve analytical calculations of the time points at which different liner modes go unstable. For these analytical studies, time-dependent parameters such as liner acceleration, effective thickness of the liner region that still remains solid, and effective

strength are obtained from 1D simulations. This study allows calculation of an upper bound on liner roughness which would prevent the growth of magnetic Rayleigh instabilities.

The high level of peak compression observed in this 1D study may not be achievable in a real system because of 2D and 3D instabilities. Two dimensional or three-dimensional studies are required to confirm this point

References

[1] Sheehey P, Faehl R, Kirkpatrick R and Lindemuth I R 2001 *Digest of Technical Papers, IEEE 13th Int. Pulsed Power Conf. (Las Vegas, USA)* (New Jersey: Institute of Electrical and Electronic Engineers) vol 2 p 1603

[2] Lindemuth I R and Kirkpatrick R 1983 *Nucl. Fusion* **23** 263

[3] Sheehey P, Atchison W, Faehl R, Kirkpatrick R, Lindemuth I R and Siemon R E 1999 *Digest of Technical Papers, IEEE 12th Int. Pulsed Power Conf. (California, USA)* (New Jersey: Institute of Electrical and Electronic Engineers) vol 2 p 888

[4] Esaulov A *et al* 2004 *Phys. Plasmas* **11** 1589

[5] Siemon R E *et al* 2005 *Nucl. Fusion* **45** 1148

[6] Subhash P V, Madhavan S and Chaturvedi S 2006 *Phys. Plasmas* **13** 072507

[7] Degnan J H *et al* 1999 *Phys. Rev. Lett.* **82** 2681

[8] Ryutov D D 2004 *Presented at the ICC Workshop (Madison, WI)*

[9] Chittenden J P 2000 The Z-pinch approach to fusion *Physics World* p 39 (May)

[10] Chittenden J P *et al* 1999 *Phys. Rev. Lett.* **83** 100

[11] Siemon R E, Lindemuth I R and Schoenberg K F 1998 Magnetized target fusion: a proof-of-principle research proposal *Technical Report* No LA-UR-98-2413 Los Alamos National Laboratory, NM, USA

[12] Vekshtin G E 1990 *Reviews of Plasma Physics* vol 15 (New York: Consultants Bureau) p 1

[13] Garanin S F, Ivanova G G, Mamyshev V I and Sofronov V N 2004 *10th Int. Conf. on Megagauss Magnetic Field Generation and Related Topic (Berlin, Germany)*

[14] Garanin S F, Mamyshev V I and Palagina E M 2004 *10th Int. Conf. on Megagauss Magnetic Field Generation and Related Topic (Berlin, Germany)*

[15] Lindemuth I R and Siemon R E 2009 *Am. J. Phys.* **77** 407–16

[16] Slutz S A, Herrmann M C, Vesey R A, Sefkow A B, Sinars D B, Rovang D C, Peterson K J and Cuneo M E 2010 *Phys. Plasmas* **17** 056303

[17] Anderson O A, Furth H P, Stone J M and Wright R E 1958 *Phys. Fluids* **1** 489

[18] Colgate S A and Furth H P 1960 *Phys. Fluids* **3** 982

[19] Vlases G C 1964 *Phys. Fluids* **7** 1358

[20] Subhash P V, Madhavan S and Chaturvedi S 2009 *Phys. Plasmas* **16** 012701

[21] Falthammer C G 1961 *Phys. Fluids* **4** 1145

[22] Jon-Erik Dahlin and Scheffel J 2004 *Phys. Scr.* **70** 310

[23] Makhin V, Siemon R E, Bauer B S, Esaulov A, Lindemuth I R, Sotnikov V I, Ryutov D D and Sheehey P T 2005 *Phys. Plasmas* **12** 042312

[24] Kadomstev B B 1966 *Reviews of Plasma Physics* (New York: Consultants Bureau) p 153

[25] Steinberg D J, Cochran S G and Guinan M W 1980 *J. Appl. Phys.* **51** 1498

[26] Krishnamurthy E V and Sen S K 1991 *Numerical Algorithms* (New Delhi, India: Affiliated Press)

[27] Burgess T J 1987 *Megagauss Technology and Pulsed Power Applications* (New York: Plenum)

[28] Chen F F 1990 *Plasma Physics and Controlled Fusion* (New York: Plenum Press)

[29] Mishra V, Pahari P, Singh G, Sakthivel N, Ikkurthi V R, Kumar R and Chaturvedi S 2006 *Proc.: Megagauss-XI Conf. (London, UK)*

[30] Eliezer S, Ghatak A and Hora H 1986 *An Introduction to Equations of State: Theory and Applications* (Cambridge: Cambridge University Press)

[31] Macfarlane J J 1989 *Comput. Phys. Commun.* **56** 259

[32] Vekhtein G E 1979 *JETP.—Lett.* **30** 596–600

[33] Subhash P V, Madhavan S and Chaturvedi S 2008 *Phys. Scr.* **77** 035501

[34] Rayevskya V A *et al* 1997 *UCRL-CR-126710: Hydrodynamic Instability in Strong Media*, University of California